RESEARCH ARTICLE

A Single Inductor Multi-Port Power Converter for Electric Vehicle Applications

SHAIK REDDI KHASIM[1], **(Member, IEEE), C. DHANAMJAYULU**[1], **(Senior Member, IEEE), AND S. M. MUYEEN**[2], **(Senior Member, IEEE)**

[1]School of Electrical Engineering, Vellore Institute of Technology, Vellore, Tamil Nadu 632014, India
[2]Department of Electrical Engineering, Qatar University, Doha, Qatar

Corresponding authors: C. Dhanamjayulu (dhanamjayulu.c@vit.ac.in) and S. M. Muyeen (sm.muyeen@qu.edu.qa)

ABSTRACT This research presents a non-isolated multi-port power converter feasible to hybridize energy alternatives in electric vehicles. Due to the hybridization of the various input sources, there are several advantages in load power distribution in the system. Flexible control of discharging as well as the charging process concerning the energy sources can be achieved. The developed converter can able to boost the voltage levels with dual inputs such as a renewable solar PV and the other input as a battery and provides dual outputs with various voltage levels, which can able to suit the converter fed for several loads like motor drive and the low-rated loads like lighting and other auxiliary supplies in electric vehicles. Also, as the various voltages appear at the output, this converter can be interfaced with multilevel inverters fed electric vehicle drivetrain. The utilization of multilevel inverters reduces the total harmonic distortion and torque ripples in motor drives in electric vehicles. The proposed converter consists of less number of components making the circuit simple and cost-effective. With one inductor, two various modes are obtained for charging and discharging states concerning the energy storage units. A state-space analysis is designed for all the converter operating modes along with its control design. The proposed multi-port DC-DC converter is designed in MATLAB/Simulink and tested in a laboratory environment with a hardware setup.
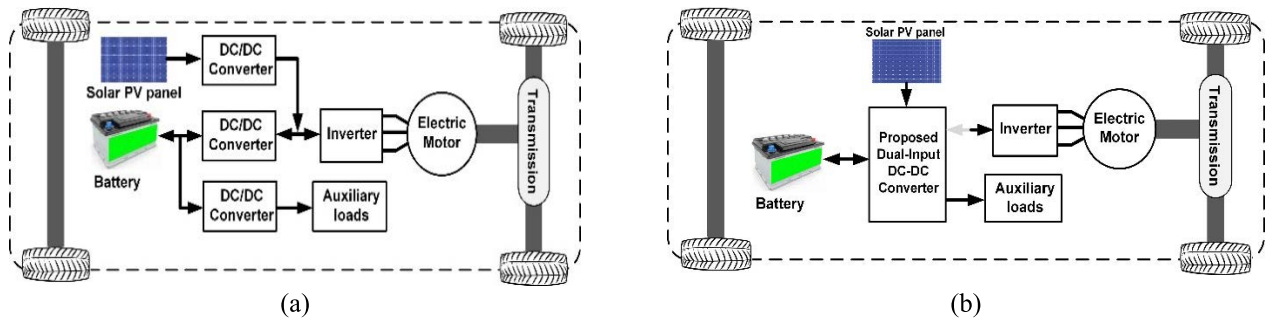
INDEX TERMS Multi-port DC-DC converters, hybrid energy storage system, state-space modeling, electric vehicles.

I. INTRODUCTION

Because of the world's rapidly increasing population and energy demand, which is raising the cost of gas and oil and reducing the availability of fossil fuels, electric vehicles (EVs) should be used instead of fossil-fuel cars. As a result, interest in developing EVs powered by clean and renewable energy sources to replace fossil-fuel vehicles has grown steadily. Electric vehicles (EVs) are a promising alternative for transportation-related applications because they can help the environment by using renewable energy sources [1], [2]. In the case of electric vehicles, the solar PV system is used as a clean energy source. Solar PV energy sources use solar energy to generate electricity. The maximum power from the solar panel was extracted using the maximum power

The associate editor coordinating the review of this manuscript and approving it for publication was Alon Kuperman.

point tracking (MPPT) technique [3], [4]. At the moment, the use of solar PV energy systems meets the requirements for electric vehicle applications. As long as the energy is available, these provide energy to the required load and charge the battery. Hence, there exist many limitations of the solar PV system such as the various irradiance levels causing the system less effective in power transfer to the load and the availability is not constant throughout the way. To overcome these constraints, a solar PV system with a secondary battery source is used to provide energy from source to load. The hybridised combination of energy storage systems provides continuous power transfer to the load and meets the load's high power requirements at high speeds and terrains [5], [6], [7], [8]. Different voltage ratings are used to interface energy storage systems such as batteries and supercapacitors. Implementing the system with individual DC-DC converters for each source makes the system bulky and complex, increasing

FIGURE 1. (a) Conventional EV powertrain representing the converter (b) EV powertrain with the proposed converter configuration.

the system's cost. As a result, a converter with multiple voltage-rated inputs is required to handle multiple energies and feed them into the system. In general, hybrid energy storage systems are interfaced with a multi-input converter, which comes in a variety of variants depending on the isolation requirement for non-isolation and isolation type DC-DC converters. FIGURE 1 depicts the general layout of the multi-input converter-fed electric motor.

In an isolated multi-port converter configuration, a high-frequency transformer is used to produce isolation between the electric constraints. This allows for efficient isolation and impedance matching on both sides of the converter. Leakage inductance is used as a storage device in isolated converters to transmit power between both sides of the converter. Isolated dc-dc converters frequently include power converters in addition to the high-frequency transformer. The transformer phase shift between the primary and secondary voltage constraints has been changed to maintain efficient power transfer from both converter ports [9], [10], [11]. There are several types of converters in this category, including half-bridge converters, full-bridge converters, and combinational multiport converters [12], [13], [14]. Because of the transformer, these are quite large. Inverters are required in these converters at the transformer's input port, with which dc can be converted to ac supply and ac can be converted to dc using the converters. As a result, various switches are used in all converter terminals, increasing the losses, and the system losses increase as transformer winding losses increase. These shortcomings are addressed in non-isolated multi-port converters, which are ideal for electric vehicle applications.

Concerning the H-bridge, a non-isolated multiport converter has been implemented [15]. In practise, various voltages can be obtained by cascading H-bridge configurations while taking into account various dc-link voltage levels. Because of the converter's coupling mechanism to multiple ports, the negative modes are not investigated [16], [17] Introduces the concept of a multiphase converter. The energy stored in the converter's energy storage sources can be absorbed as well as delivered to the load. There exists an individual inductor for each source and hence this is considered a drawback of the converter [18], [19], [20] also cost-efficient three-port converter for EV/HEV applications is proposed.

The author offers a three-input converter for the connection of batteries, solar cells, and fuel cells [21]. You can charge and discharge the battery from various sources and loads with proper converter switching. Reference [22] Presents a systematic method for designing non-isolated topologies using a combination of buck, boost, sepic, and cuk type converters. There are two types of converters described: PVSC and PCSC, which are pulsing voltage and current sources. As a voltage source, PVSC can be connected in series with an inductor to form a double input converter. Because the PCSC is a current source, it may be used to build a double-input converter by connecting it in series with a capacitor. In [20], the energy management strategy among the various inputs like battery, SC and the electric motor is suggested for use in an electric automobile. Here, instead of employing two separate inductors as energy storage components are used. When compared to two independent inductors, it is claimed that employing the inductors with coupling can able to save 22–26% in volume. In contrast, connected inductors have a larger volume than a single inductor. This converter can also regenerate braking energy to the battery and SC. Reference [23] proposes transferring load power across input sources using a multiport converter with a single inductor. This converter can also be used to transfer power from one source to another. In [24], the author introduced a novel zero voltage switching DC-DC converter. The layout of conventional converters utilized in electric vehicles is represented in FIGURE 2 (a) whereas the proposed converter configuration is represented in FIGURE 2 (b).

Connected inductors, on the other hand, have a larger volume than a single inductor. This converter also allows for the regeneration of braking energy to the battery and SC. Reference [23] suggests transferring load power across input sources using a multiport converter with a single inductor. This converter can also be used to transfer power between sources. References [25] and [26] offer a multi-port con verter that may create numerous voltages at its output sections and these are the preset values regardless of the variation of the load power and input voltage interfaced with PV systems. Reference [27] Presents a novel multi-output buck converter control technique that delivers suitable dynamic performance. However, this converter is worthless in applications like

electric cars, where various input energy excitations like solar and a battery are utilized. This can be solved by incorporating multi-port converters. Reference [28] Describes a non-isolated high step-up multi-port converter and its performance evaluation using a variety of parameters. References [29] and [30] evaluate the MPPT of a solar PV converter under partial shading conditions. Another flaw in the proposed converter is its inability to transmit energy across input sources.

A multi-port non-isolated converter is suggested in this work, which is based on the mixture design of multiple inputs and outputs of the converter. In comparison to previous scenarios, the suggested converter contains fewer components. This converter can regulate the flow of electricity between sources and loads. Furthermore, the suggested converter includes many outputs, each of which can have a different voltage level.

The remainder of the paper is presented as follows. Section II provides the modeling of solar PV and MPPT. Section III explains the construction and modes of operation of the developed converter. The dynamic modeling is shown in Section IV. Whereas the control architecture of the converter is discussed in section V. Both simulation and experimental results are discussed in Sections VI and the article is concluded in Section VII.

II. MODELING OF PV ARRAY
The model of a solar PV cell plays a prominent role in understanding a solar PV system. FIGURE 1 shows the developed circuit in its entirety, which includes solar PV, a type of dual input multi-port DC-DC converter. Analogous circuits with I-V and P-V aspects, irradiance and temperature effects, and partial shading circumstances are all models that may be used to describe this. Photonic energy is denoted by photo, while voltaic energy is denoted by voltaic, meaning that photonic energy drawn from the sun is transformed into electric energy [31]. Solar modules are made up of various modules with respective solar cells. Reference [32] Utilizes P-N semiconductor diodes. The output of developed solar PV tends to alter as temperature and ambient conditions change [33]. As a result, consider the following aspects when modeling a solar PV system. The internal resistance R_s and R_p are linked in series and parallel to the diode in a solar cell, which is known as an analogous circuit depicted in FIGURE 2.
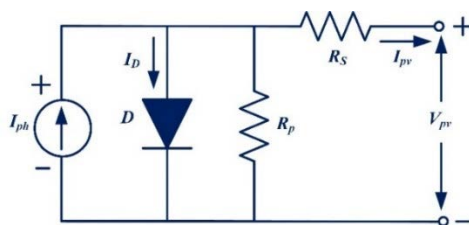
FIGURE 2. A solar cell's equivalent circuit.

The internal resistance R_s and R_p are linked in series and parallel to the diode in a solar cell, which is known as an

analogous circuit depicted in Fig. 2.

$$I_{PV} = \left\{ I_P - I_0 \left[exp \left(\frac{q(V_{PV} + R_S I_{PV})}{N_S ATK} \right) - 1 \right] \right. \left. - \frac{(V_{PV} + R_S I_{PV})}{N_S R_P} \right\} \quad (1)$$

The series and parallel resistances are Rs and Rp, respectively, and the count of PV cells connected in both series and parallel respectively are N_s and N_p. K represents the Boltzmann constant (1.3806503102 J/K), T gives the temperature, A is the semiconductor device's ideality factor, and I_{ph} is the obtained current, which is dependent on the respective irradiation and nominal temperature stated in equation (2)

$$I_P = [I_{SOC-STC} + K_i (T - T_{STC})] - \left(\frac{G}{G_{STC}} \right) \quad (2)$$

$I_{SOC-STC}$ is a short circuit current (SCC) under basic operating and testing conditions (STC), K_i represents the coefficient of SCC, G (in W/m^2) provides the respective irradiation of the solar cell, G_{STC} (1000W/m^2) provides the irradiation at STC, and T_{STC} (25°C) is the cell temperature at STC.

$$I_O = \left\{ \frac{I_{SOC-STC} + K_i (T - T_{STC})}{exp \left[(V_{OCV-STC} + K_V (T - T_{SCC}) / AV_{th}) \right]} \right\} \quad (3)$$

where $V_{VOCV-STC}$ denotes the open-circuited voltage (OCV) provided at STC, K_v denotes the OCV coefficient and V_{th} denotes the cell's thermal equivalent voltage and these values may be found on the module's datasheet.

$$P_{PV} = V_{PV} \times N_P \left(I_{Ph} - I_O exp \left(\frac{qV_{PV}}{N_S AKT} \right) - \left(\frac{V_{PV}}{N_S} \right) \right) \quad (4)$$

Fig. 3 depicts the I-V/P-V properties of a solar cell. Representation of a graph shows the operating point of a solar PV is inherently unstable, varying constantly from zero to OCV. The maximum power point is a single point in this process that produces maximum power based on the specified design of the solar module at varying irradiance and temperatures (MPP). V_{MPP}, and I_{MPP} are the relative voltages and currents at this moment, as indicated in FIGURE 3.
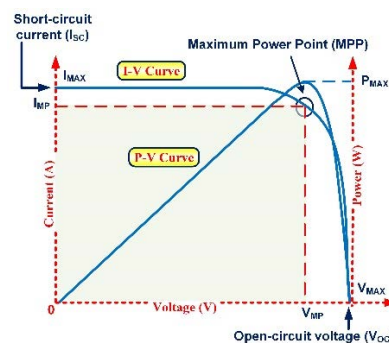
FIGURE 3. Solar Cell I-V Characteristics.

Irradiance, temperature, and the quantity of series-connected strings and parallel-connected strings all influence

the voltage and current generated by the PV array. As a result, it is necessary to make an informed decision on the sort of solar panel to choose. 1Soltech 1STH-215-P panel is considered from available data of the solar modules in MATLAB with 2 parallel strings and 2 series modules connected for one string in this work. Table 1 lists the characteristics of the chosen solar panel, as well as the readings for one parallel-connected string and one series module at 1000 W/m^2 irradiance and a temperature of 250°C.

A. MPPT CONTROLLER

The maximum power varies based on the environment's temperature and irradiance. MPPT with a real-time implementation is an essential component of any solar module system since the maximum accessible energy of solar cells fluctuates concerning the weather. The developed MPPT approaches may be divided into three classes in the technical literature 10: Techniques concerning artificial intelligence, methods concerning direct methods, and ways based on indirect methods.

The MPP is found using direct procedures, also known as genuine searching methods, which include repeatedly perturbing the PV array's operational point. In this section, the MPPT schemes widely utilized are Hill Climbing HC, Perturb and Observe P&O and Incremental Conductance INC in PV systems. The P&O approach comprises analyzing the operating voltage of PV to achieve the MPP. The respective duty cycle of the developed converter is affected by hill-climbing methods, such as the P&O scheme [14]. Although these technologies are characterized by their simplicity, they are limited to low-rated applications due to their steady state. The steady-state oscillation can be reduced utilization of the incremental conductance technique can decrease steady-state oscillation since the plot representing the power versus voltage at the MPP is zero. ANN and indirect approaches have been developed to increase the dynamic behavior and performance of the MPPT. Artificial intelligence techniques that focus on the nonlinear features of PV arrays provide a speedy but computationally challenging solution to the MPPT issue. The indirect methods function by calculating the array's MPP based on the output characteristics. The open-circuit voltage OCV and the short-circuit current SCC approaches can be used to compute the MPP. The specifications of the solar PV module are represented in TABLE 1.

TABLE 1. Parameters of 215W solar panel.

Open circuit voltage (V$_{oc}$)	36.3V
The voltage at maximum power point (V$_{MPP}$)	34V
The voltage at maximum power point (V$_{MPP}$)	35V
Short circuit current (I$_{sc}$)	7.84A
Maximum power	213.15W
Diode saturation current (I$_O$)	2.9259×10^{-10}A
Current at maximum power point (I$_{MPP}$)	7.35A
Diode ideality factor	0.98117

B. MPPT WITH ARTIFICIAL NEURAL NETWORK

This article uses an ANN to track the greatest PowerPoint. A three-layer ANN is employed to get to MPP, as illustrated in FIGURE 4.

The ANN's input variables are temperature T and irradiance G, whereas the output variable is MPP voltage V$_{mpp}$. Some data must be acquired as input as well as the output variables for training. The neuron weights in distinct levels are therefore calculated as a consequence. The solar PV data can be collected and programmed in MATLAB. ANN may be taught in several different methods. The backpropagation approach is used for training the error of ANN in this article.
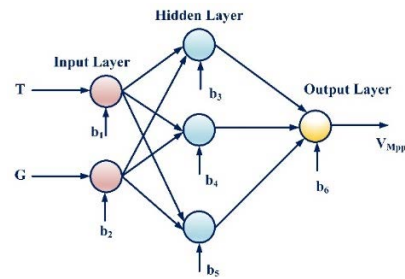

FIGURE 4. The structure of a neural network.

Once the training of the ANN is completed the neuron weights are to be specified such as the V$_{mpp}$ is the output of the ANN for the input values of T and G. Using the V-I characteristic of the modeled PV, the current at the MPPT I$_{mpp}$ can now be calculated. As a result, multiplying V$_{mpp}$ and I$_{mpp}$ yields maximum power _P$_{max}$_.

The PV and the MPPT tracker shown in Fig. 4 are made up of a converter and an ANN-based control unit. The following equation is used to manage a chopper with a particular V$_{mpp}$ and I$_{mpp}$ duty cycle at any given time:

$$D = 1 - \sqrt{\frac{V_{mpp}}{I_{mpp}} \times \frac{I_o}{V_0}} \qquad (5)$$

III. PROPOSED DC-DC CONVERTER

A multi-port converter is developed with a single inductor four switches S$_1$, S$_2$, S$_3$, S$_4$ and four diodes D$_1$, D$_2$, D$_3$, D$_4$ along with two capacitors C$_1$ and C$_2$. The converter is excited with two input energy storage sources such as a solar PV input V$_{pv}$ and battery input V$_{bat}$. As one input energy source cannot able to feed the power requirement in an electric vehicle, the requirement of two energy sources is essential. The proposed double input and double output type converter are shown in FIGURE 5 [23]. The power fed to the developed converter by using the two input energy sources has been analysed using the load resistances R$_1$ and R$_2$. The effective switching of the converter is controlled by the power flow among the input energy sources and load resistances by enhancing the
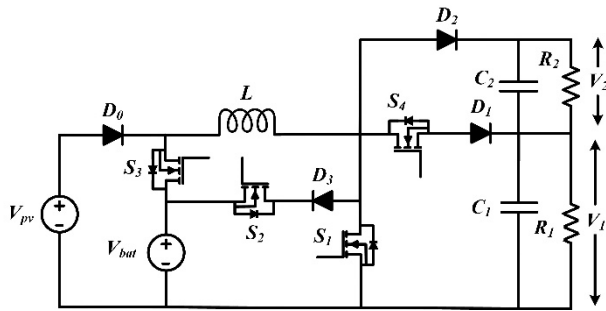
FIGURE 5. Proposed multi-port converter with two inputs and two outputs [23].

input voltages. The output voltages can be changed concerning the multilevel inverter input voltages.

With the interfacing solar PV energy source with a battery, the proposed converter is well suited for its robustness. The power feeding from the respective sources along with the load utilizing the proposed circuit components is represented in FIGURE 5. The load resistances R1 and R2 can be modeled concerning the equivalent resistance of the motor and the multilevel inverter input voltages. The proposed converter is capable of interfacing with various multilevel inverters. The multilevel inverters require asymmetrical voltage source requirements which can be fed with the proposed converter. The four switches can able to regulate the flow of power among the sources to the output voltages and makes the voltages more flexible with the multilevel inverter.

In the proposed converter the source V_{pv} delivers power to V_{bat} and charges the battery but V_{bat} sources do not feed the power to source V_{pv}. In the case of electric vehicle applications, solar PV cannot be charged from the battery and the battery is charged from an external source or solar PV source. In this article, solar PV can be utilized as a prominent source of the system and the battery is the energy storage system device. Concerning the power utilization of the battery and state of charge, there exist two operating modes of the developed converter. For all modes of the converter, one switch is inactive by activating the three switches. Both input sources are active and feed the power at high load power requirements. During this mode of operation, switches S_1, S_3, and S_4 are active and feed the power to the load and switch S_2 is inactive. In the case when the load power requirement is less, the V_{bat} will be charged from the source V_{pv} and the only source V_{pv} supplies the energy to the load. In this condition, the switches S_1, S_2, and S_4 become an active state and switch S_3 is in an off state. As the output voltage is dependent on the current obtained from the converter, power should be balanced from the input powers to the load and the ripple current drawn needs to be reduced. Hence for these requirements, the steady-state and dynamic activity has been analyzed in the continuous conduction mode (CCM).

In the low power requirement mode, when the required current is drawn is less and the battery is getting charged, it is feasible to operate the converter in discontinuous conduction mode (DCM). Hence, this model is analyzed in section IV. The analysis is done in such a way that each input source is analyzed separately. The converter in one mode can be considered as a single input operation. There exist two major operations of the converter such as battery discharging mode and charging mode which are represented in detail are represented below.

A. BATTERY DISCHARGING MODE

During this mode, the loads are supplied by two input power sources V_{pv} and V_{bat}. The switches S_1, S_3, S_4 are active and feed the power to the load and the switch S_2 is inactive. Every switch has its operation in process of power delivered from source to load. S_1 adjusts the current through the battery to a required value by altering the current through the inductor. The switch S_3 keeps the total output voltage $V_T = V_{pv} + V_{bat}$ at a constant level. The voltage output V_{pv} is also controlled by the switch S_4. The adjustment of V_T and V_{pv} affects the output voltage V_{bat}. FIGURE 7 represents inductor voltage and current waveforms, as well as the gate signals of switches. There exist four different operation modes in a single switching period:

1) SWITCHING CONDITION 1 ($0 < t < D_3T$)

During this operation, the switches S_1 and S_3 are active. Due to the diodes D_1 and D_2 being in reverse bias when S_1 is switched on, switch S_4 is inactive. Diode D_0 is in reverse bias since S_3 is ON. FIGURE 6(a) represents the equivalent model of the developed converter. Here, V_{bat} charges the inductor L, which causes the current through the inductor to rise. The capacitors C_1 and C_2 can able to deliver energy to the load resistances R_1 and R_2 by discharging. The respective equations of the inductor and capacitors are represented below in equation (6).

$$L\frac{di_L}{dt} = V_{pv}$$
$$C_1\frac{dV_1}{dt} = -\frac{V_1}{R_1}$$
$$C_2\frac{dV_2}{dt} = -\frac{V_2}{R_2} \qquad (6)$$

2) SWITCHING CONDITION 2 ($D_3T < t < D_1T$)

During this operation, switch S_1 remains active while switch S_3 is inactive. Switch S_4 remains off when S_1 is switched on because the respective diodes D_1 and D_2 are in reverse bias. The equivalent circuit model of the developed converter is represented in FIGURE 6(b). During this mode, V_{pv} charges the inductor L and increases the current through the inductor. Additionally, the respective capacitors C_1 and C_2 are getting discharged supplying the energy stored to the R_1 and R_2 load resistances respectively. The equations of the capacitors and
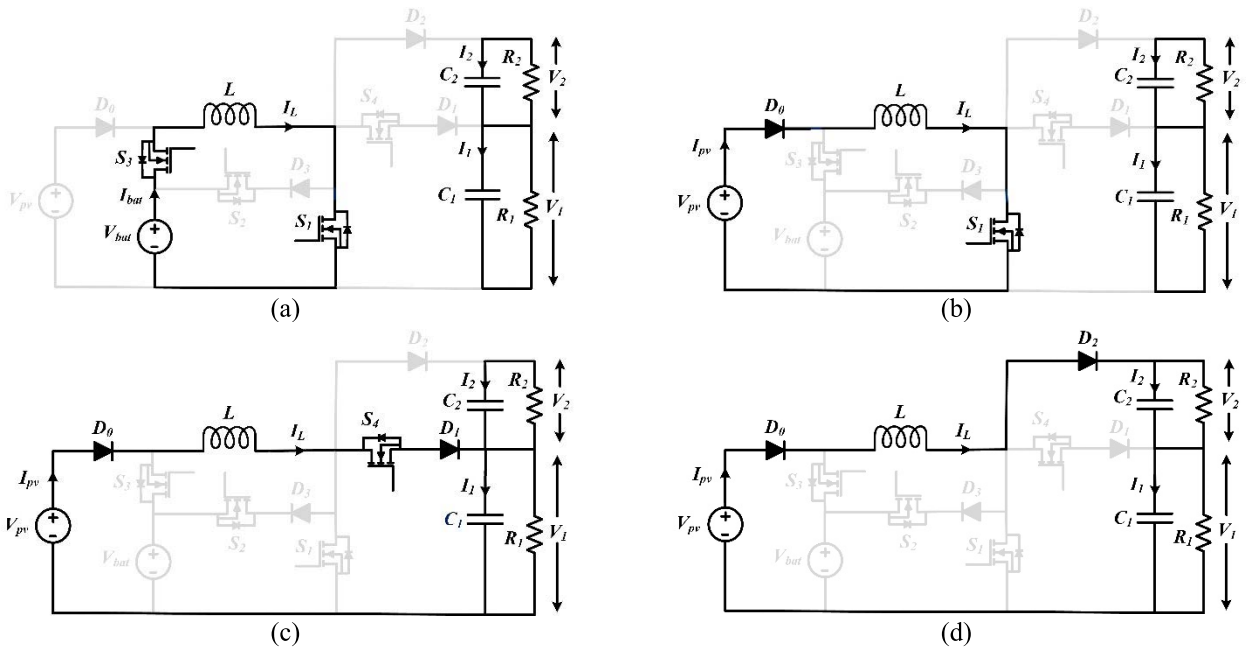
FIGURE 6. Battery discharging modes: (a) Mode-1 (b) Mode-2 (c) Mode-3 (d) Mode-4.
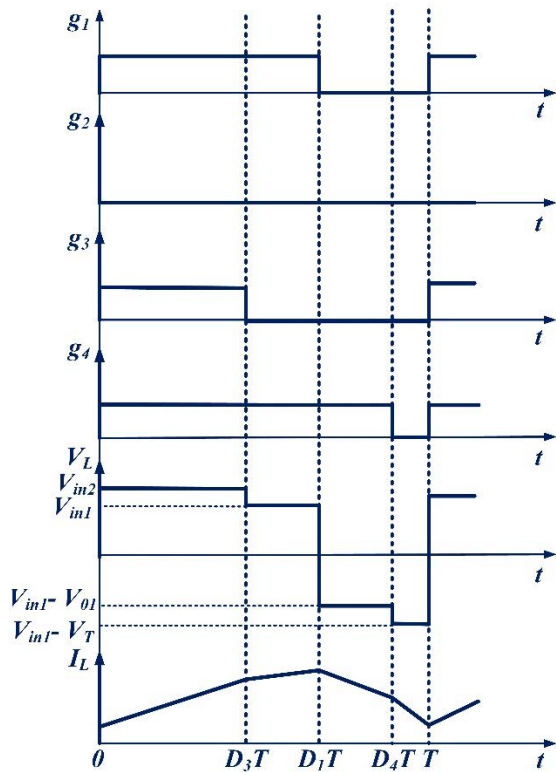

FIGURE 7. Typical steady-state waveform while discharging a battery.

inductors during this operation specifically are represented below in equation (7).

$$L \frac{di_L}{dt} = V_{pv}$$

$$C_1 \frac{dV_1}{dt} = -\frac{V_1}{R_1}$$

$$C_2 \frac{dV_2}{dt} = -\frac{V_2}{R_2} \tag{7}$$

3) SWITCHING CONDITION 3 ($D_1T < t < D_4T$)

During this operation, switch S_1 is inactive, while switch S_3 is still turned off with the switch S_4 is active. The diode D_2 is in reverse bias. FIGURE 6(c) represents the analogous circuit model of the developed converter. The inductor gets discharged by storing the energy which can be distributed to the load with C_1 and R_1 leading to a decrease in inductor current. In this condition, the capacitor C_1 is getting charged, while C_2 is discharged, supplying the energy stored to the load resistance R_2. The equations of the capacitors and inductor during this operation specifically are represented below in equation (8).

$$L \frac{di_L}{dt} = V_{pv} - V_1$$

$$C_1 \frac{dV_1}{dt} = i_L - \frac{V_1}{R_1}$$

$$C_2 \frac{dV_2}{dt} = -\frac{V_2}{R_2} \tag{8}$$

4) SWITCHING CONDITION 4 ($D_4T < t < T$)

During this operation, all switches become inactive. As a result, diode D_2 is in forwarding bias. The inductor L gets discharged by storing the energy supplied to the capacitors C_1 and C_2 with the R_1 and R_2 load resistances. The capacitors C_1 and C_2 are getting charged. The analogous circuit model of the developed converter is represented in FIGURE 6(d). The equations of the capacitors and inductors during this

operation specifically are represented below in equation (9).

$$L\frac{di_L}{dt} = V_{pv} - (V_1 + V_2)$$
$$C_1\frac{dV_1}{dt} = i_L - \frac{V_1}{R_1}$$
$$C_2\frac{dV_2}{dt} = i_L - \frac{V_2}{R_2} \quad (9)$$

B. BATTERY CHARGING MODE

During the mode of operation, V_{pv} feeds loads by providing power to V_{bat}. This situation appears in the case where the load-rated power is less and the battery gets charged. During this condition, switches S_1, S_2 and S_4 are operational, while switch S_3 is inactive. This mode, like the converter in the above mode of operation, takes into account a set duty for each switch. The total output voltage, $V_T = V_{pv} + V_{bat}$ to be adjusted to the appropriate level by turning on S_1. Switch S_2 keeps the battery charging current (I_{bat}) at a required level. The voltage output V_{pv} is likewise accessed by the switch S_4. The modification of V_T and V_{pv} controls the voltage output V_{bat}. FIGURE 8 represents the gate switching signals of switches as well as the waveforms representing the voltage and current of the inductor. As per the distinct switch states, the four alternative operating modes exist in one switching period addressed below.
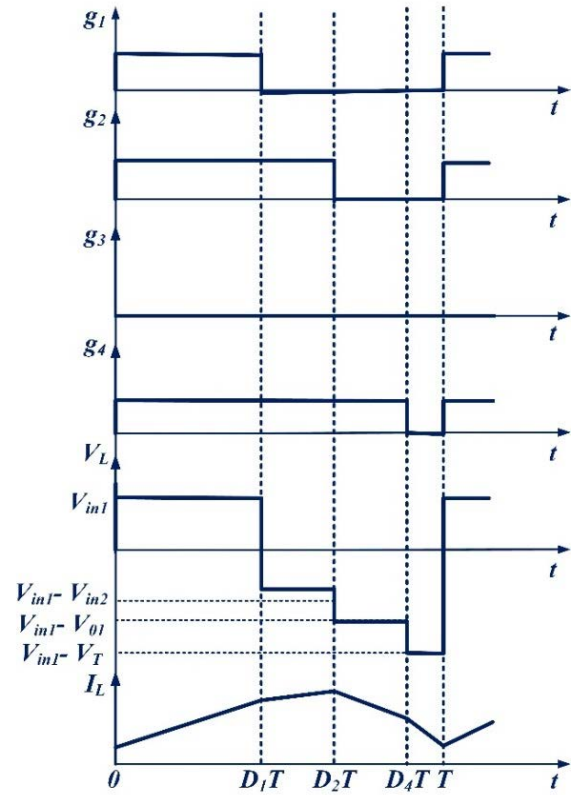
1) SWITCHING CONDITION 1 ($0 < t < D_1T$)

During this mode of operation, the switch S_1 is active causing S_2 and S_4 to be in reverse bias and inactive. Furthermore, because the diode D_2 is reverse-biased, it does not conduct. FIGURE 9(a) represents the analogous circuit model of the developed converter operating in this mode. V_{pv} charges inductor L increasing the inductor current. Where the capacitors of C_1 and C_2 get discharged by supplying the energy stored to R_1 and R_2 load resistances. The equations of the capacitors and inductors during this operation specifically are represented below in equation (10).

$$L\frac{di_L}{dt} = V_{pv}$$
$$C_1\frac{dV_1}{dt} = -\frac{V_1}{R_1}$$
$$C_2\frac{dV_2}{dt} = -\frac{V_2}{R_2} \quad (10)$$

2) SWITCHING CONDITION 2 ($D_1T < t < D_2T$)

During this mode, the switch S_1 becomes inactive, while the switch S_2 is turned on. As the diodes D_1 and D_2 are in reverse bias, S_4 is inactive. FIGURE 9(b) represents the circuit of the developed converter. Since the inductor current falls over this period, and inductor distributes its energy stored to the battery V_{bat}. The capacitors C_1 and C_2 are discharged in this mode, delivering the energy stored to R_1 and R_2 load resistances respectively. The equations of the capacitors and inductors during this operation specifically are represented

FIGURE 8. The typical steady-state waveform in the charging mode of a battery.

below in equation (11).

$$L\frac{di_L}{dt} = V_{pv} - V_{bat}$$
$$C_1\frac{dV_1}{dt} = -\frac{V_1}{R_1}$$
$$C_2\frac{dV_2}{dt} = -\frac{V_2}{R_2} \quad (11)$$

3) SWITCHING CONDITION 3 ($D_2T < t < D_4T$)

During this mode, the switch S_1 and switch S_2 become inactive and the switch S_4 is switched on in this state. The diode D_2 is reverse bias. The circuit of the developed converter is depicted in FIGURE 9(c). The Inductor gets discharged and distributes its energy stored to C_1 and R_1, resulting in a drop in inductor current. The capacitors C_1 and C_2 are charged with a capacitor C_2 is discharged, delivering its energy stored to the R_2 load resistance. The equations of the capacitors and inductors during this operation specifically are represented below in equation (12).

$$L\frac{di_L}{dt} = V_{pv} - V_1$$
$$C_1\frac{dV_1}{dt} = i_L - \frac{V_1}{R_1}$$
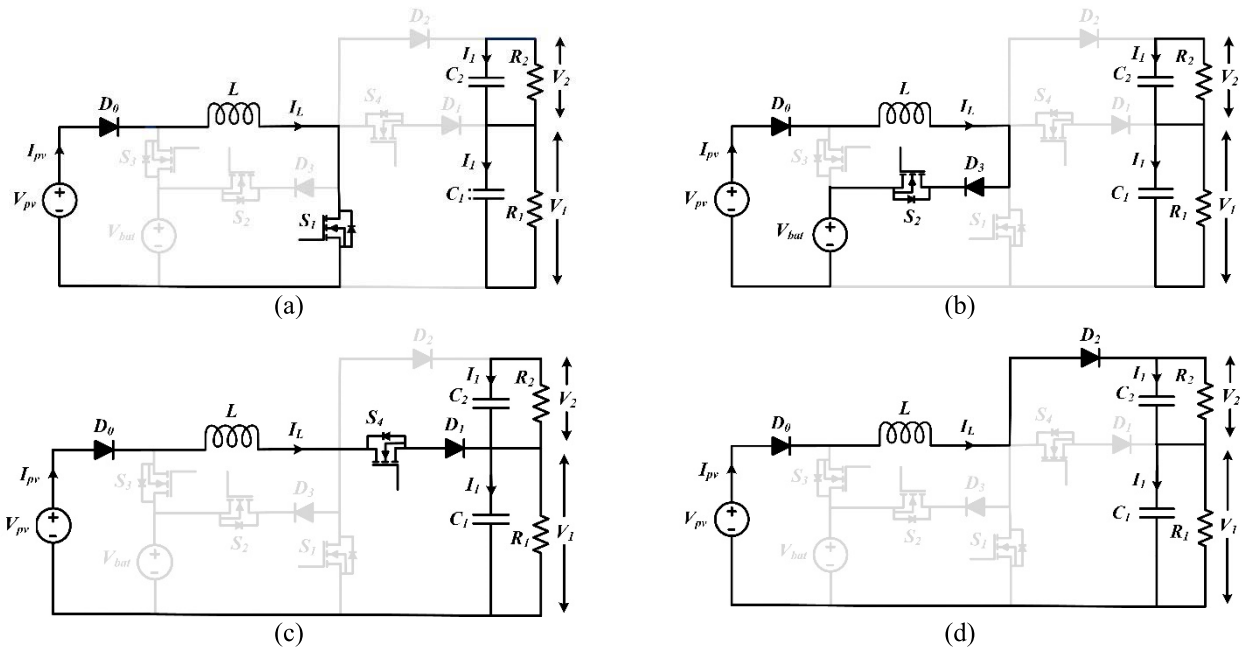$$C_2\frac{dV_2}{dt} = -\frac{V_2}{R_2} \quad (12)$$

FIGURE 9. Battery charging modes: (a) Mode-1 (b) Mode-2 (c) Mode-3 (d) Mode-4.

4) SWITCHING CONDITION 4 ($D_4T < t < T$)

During this mode, all the switches become inactive. As a result, the diode D_2 is in forward bias. The circuit of the developed converter is depicted in FIGURE 9(d). The inductor gets discharged in this condition and the stored energy is delivered to the capacitors C_1 and C_2 as well as R_1 and R_2 load resistances. The charging of the capacitors C_1 and C_2 can be made. The equations of the capacitors and inductor during this operation specifically are represented below in equation (13).

$$L\frac{di_L}{dt} = V_{pv} - (V_1 + V_2)$$
$$C_1\frac{dV_1}{dt} = i_L - \frac{V_1}{R_1}$$
$$C_2\frac{dV_2}{dt} = i_L - \frac{V_2}{R_2} \qquad (13)$$

IV. DESIGNING OF THE PROPOSED CONVERTER

A. DYNAMIC MODELLING

The suggested converter can able to be controlled by switches S_1, S_2, S_3 and S_4 as indicated in the previous section. Each switch has a distinct function. Output voltages and battery charging or discharging current can be adjusted by properly regulating switch duty cycles. The converter's closed-loop controller must first be designed using a dynamic model. As previously stated, the developed converter has two major modes of operation: while the battery discharge, two inputs supply energy to load and in the case of charging the battery the source V_{pv} not only delivers load-rated power but it charges V_{bat}. For each of the converter's operation modes,

there are several dynamic models. As a result, distinct controllers must be created for each mode of operation.

1) BATTERY DISCHARGING MODE

The basis for optimal controller design is the small-signal model. An effective model will be especially useful for such a multi-port converter to achieve closed-loop-based control importantly for optimizing the dynamics of the converter. The multiport converter, unlike ordinary consisting of single input and output converters of a high-order type system, represents derivation of transfer functions is time-consuming; as a result, obtaining values of the respective zeros and poles for the analysis is a challenging task. However, the dynamics of the plant can be expressed as a matrix, which necessitates the use of computer software to draw bode plot graphs of various transfer functions. The duty ratios, state variables and input energy excitations have two components dc values (X, D, V) and the respective perturbations (x, d, v), according to the small-signal modeling approach [30]. The perturbations are expected to be minor and do not fluctuate much over a single switching time. Hence the developed converter has the following equation, where the state variables are inductor current $i_L(t)$ and the respective capacitor voltages $V_1(t)$ and $V_2(t)$. The small-signal equations are derived by substituting (14) into (6)–(9), applying making to four state equations multiplied by the values of the respective duty cycle ignoring second-order terms:

$$i_L(t) = I_L + \hat{I}_L(t)$$
$$V_1(t) = V_1 + \hat{V}_1(t)$$
$$V_2(t) = V_2 + \hat{V}_2(t)$$

$$d_1(t) = D_1 + \hat{d}_1(t)$$
$$d_2(t) = D_2 + \hat{d}_2(t)$$
$$d_3(t) = D_3 + \hat{d}_3(t)$$
$$d_4(t) = D_4 + \hat{d}_4(t) \tag{14}$$

$$L\frac{d\hat{I}_L(t)}{dt} = (V_{bat} - V_{pv})\hat{d}_3(t)$$
$$+ \hat{D}_3\hat{V}_{bat}(t) + (1 - D_3)\hat{V}_{pv}(t)$$
$$- (1 - D_1)\hat{V}_1(t)$$
$$+ (D_4 - 1)\hat{V}_2(t) + V_1\hat{d}_1(t) + V_2\hat{d}_4(t)$$

$$C_1\frac{d\hat{V}_1(t)}{dt} = -I_L\hat{d}_1(t) + (1 - D_1)\hat{I}_L(t) - \frac{\hat{V}_1(t)}{R_1})$$

$$C_2\frac{d\hat{V}_2(t)}{dt} = -I_L\hat{d}_4(t) + (1 - D_4)\hat{I}_L(t) - \frac{\hat{V}_2(t)}{R_2} \tag{15}$$

As a result, the system is described in a matrix by utilizing an approach of a state-space type model, with state variables $i_L(t)$, $V_{pv}(t)$ and $V_{bat}(t)$. The state-space model is as follows:

$$\frac{dX}{dt} = AX + BU$$
$$Y = CX + DU \tag{16}$$

where X denotes the state variables, U denotes the control inputs $d_1(t)$, $d_3(t)$, and $d_4(t)$, and Y denotes the system outputs $V_{pv}(t)$, $V_T(t)$ and $i_b(t)$. As a result, the matrices like X, Y and U take the below type:

$$X = \begin{bmatrix} \hat{I}_L(t) \\ \hat{V}_1(t) \\ \hat{V}_2(t) \end{bmatrix}, Y = \begin{bmatrix} \hat{V}_1(t) \\ \hat{V}_T(t) \\ \hat{I}_b(t) \end{bmatrix}, U = \begin{bmatrix} \hat{d}_4(t) \\ \hat{d}_3(t) \\ \hat{d}_1(t) \end{bmatrix}. \tag{17}$$

Using (15) and state equations (16) to fill in the A, B, C, and D matrices, the following result is obtained:

$$A = \begin{bmatrix} 0 & \frac{(D_1-1)}{L} & \frac{(D_4-1)}{L} \\ \frac{(1-D_1)}{C_1} & -\frac{1}{R_1C_1} & 0 \\ \frac{(1-D_4)}{C_2} & 0 & -\frac{1}{R_2C_2} \end{bmatrix}$$

$$B = \begin{bmatrix} \frac{V_2}{L} & \frac{V_1}{L} & \frac{(V_{bat}-V_{pv})}{L} \\ 0 & -\frac{I_L}{C_1} & 0 \\ -\frac{I_L}{C_1} & 0 & 0 \end{bmatrix}$$

$$C = \begin{bmatrix} 0 & 1 & 0 \\ 0 & 1 & 1 \\ D_3 & 0 & 0 \end{bmatrix}, \quad D = \begin{bmatrix} 0 & 0 & 0 \\ 0 & 0 & 0 \\ 0 & I_L & 0 \end{bmatrix} \tag{18}$$

where V_{pv} and V_{bat} are the respective voltages of the given input energy sources. V_1 and V_2 are output voltages as well. Except for the duty cycle of switches D_1, D_3, D_4 and the inductor current I_L, all parameters in A, B, C, and D matrices are known. The following equation can be used to calculate the inductor current:

$$I_L = \frac{I_b}{D_3} \tag{19}$$

where I_b is the current drawn by the battery D_1, D_3, and D_4 are the only unknown parameters of stated matrices. The duty

cycles of the switches are obtained with steady-state equations represented as follows:

$$\begin{bmatrix} V_1 & V_{bat} - V_{pv} & V_2 \\ R_1I_b & V_1 & 0 \\ 0 & V_2 & R_2I_b \end{bmatrix}\begin{bmatrix} D_1 \\ D_3 \\ D_4 \end{bmatrix} = \begin{bmatrix} V_1 + V_2 - V_{pv} \\ R_1I_b \\ R_2I_b \end{bmatrix} \tag{20}$$

As a result of the above matrix equation, the duty cycles of the respective switches are calculated and presented in the A, B, C, and D matrices. The three control variables $d_1(t)$, $d_3(t)$, and $d_4(t)$ in system small-signal models (t) the state variables. The small-signal model yields the following transfer function matrix for the converter:

$$G = C(SI - A)^{-1}B + D \tag{21}$$

where

$$y = Gu \tag{22}$$

The control variables count is indicated by the rank of the transfer function matrix, G in this study is 3 depending on the number of control variables and (17).

$$\begin{bmatrix} y_1 \\ y_2 \\ y_3 \end{bmatrix} = \begin{bmatrix} g_{11} & g_{12} & g_{13} \\ g_{21} & g_{22} & g_{23} \\ g_{31} & g_{32} & g_{33} \end{bmatrix}\begin{bmatrix} u_1 \\ u_2 \\ u_3 \end{bmatrix} \tag{23}$$

where g_{ij} denotes the transfer function among y_i and u_j, and y and u are the respective system output and input vectors. As a result, there are three transfer functions:

$$\frac{\hat{V}_1(s)}{d_4(s)} = g_{11}$$

$$\frac{\hat{V}_T(s)}{d_3(s)} = g_{22}$$

$$\frac{\hat{I}_b(s)}{d_1(s)} = g_{23} \tag{24}$$

2) BATTERY CHARGING MODE

The switches S_1, S_2 and S_4 become on state, while switch S_3 is inactive, during this mode of operation, the developed converter, in which V_{pv} supplies energy to loads and V_{bat}. The first small-signal model can be created by putting (14) into (10)–(13) by applying the analysis to four state equations respectively multiplied by the values of the corresponding duty cycles by then ignoring the second-order terms, resulting in small-signal equations represented below:

$$L\frac{d\hat{I}_L(t)}{dt} = \hat{V}_{pv}(t) + V_{bat}\hat{d}_1(t)$$
$$+ (D_1 - D_2)\hat{V}_{bat}(t) + (V_1 - V_{bat})\hat{d}_2(t)$$
$$+ V_2\hat{d}_4(t) + (D_2 - 1)\hat{V}_1(t) - (1 - D_4)\hat{V}_2(t)$$

$$C_1\frac{d\hat{V}_1(t)}{dt} = -I_L\hat{d}_2(t) + (1 - D_1)\hat{I}_L(t) - \frac{\hat{V}_1(t)}{R_1}$$

$$C_2\frac{d\hat{V}_2(t)}{dt} = -I_L\hat{d}_4(t) + (1 - D_4)\hat{I}_L(t) - \frac{\hat{V}_2(t)}{R_2} \tag{25}$$
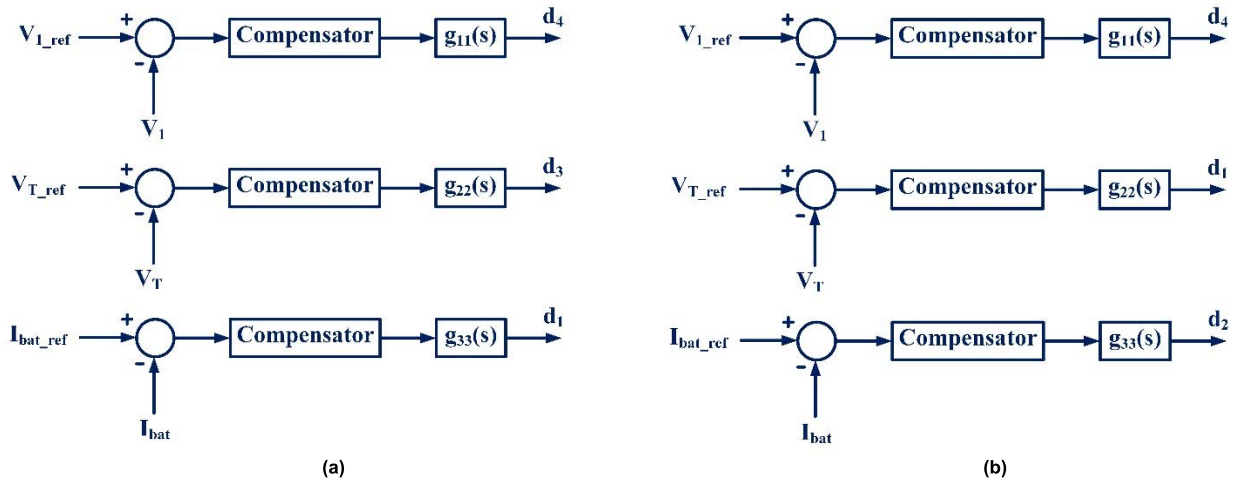
FIGURE 10. The control scheme of the developed converter (a) Discharging mode (b) Charging mode.

State-space equations can be used to express these equations. The state variables in this operation mode, which is comparable to the discharging mode of a battery with $i_L(t)$, $V_1(t)$, and $V_2(t)$. The following are examples of state variables, input and output matrices:

$$X = \begin{bmatrix} \hat{I}_L(t) \\ \hat{V}_1(t) \\ \hat{V}_2(t) \end{bmatrix}, y = \begin{bmatrix} \hat{V}_1(t) \\ \hat{V}_T(t) \\ \hat{I}_b(t) \end{bmatrix}, u = \begin{bmatrix} \hat{d}_4(t) \\ \hat{d}_1(t) \\ \hat{d}_2(t) \end{bmatrix}. \quad (26)$$

where $VT(t) = V_1(t) + V_2(t)$. Hence for this mode, there exists the matrices A, B, C and D represented below:

$$A = \begin{bmatrix} 0 & \frac{(D_2-1)}{L} & \frac{(D_4-1)}{L} \\ \frac{(1-D_2)}{C_1} & -\frac{1}{R_1C_1} & 0 \\ \frac{(1-D_4)}{C_2} & 0 & -\frac{1}{R_2C_2} \end{bmatrix}$$

$$B = \begin{bmatrix} \frac{V_{bat}}{L} & \frac{(V_1-V_{bat})}{L} & \frac{V_2}{L} \\ 0 & -\frac{I_L}{C_1} & 0 \\ 0 & 0 & -\frac{I_L}{C_1} \end{bmatrix}$$

$$C = \begin{bmatrix} 0 & 1 & 0 \\ 0 & 1 & 1 \\ D_2 - D_1 & 0 & 0 \end{bmatrix}, D = \begin{bmatrix} 0 & 0 & 0 \\ 0 & 0 & 0 \\ -I_L & I_L & 0 \end{bmatrix}$$

$$(27)$$

Except for the duty cycle of switches D_1, D_2, D_4 and the dc value of inductor current I_L, all parameters in the aforementioned matrices are known. The following equation applies to the inductor current:

$$I_L = \frac{I_b}{D_2 - D_1} \quad (28)$$

where I_b is the desired battery current value. D_1, D_2 and D_4 are the unknown parameters of stated matrices. Steady-state equations are used to calculate the duty cycle of switches.

$$\begin{bmatrix} V_{bat} & V_1 - V_{bat} & V_2 \\ -V_1 & V_1 + R_1 I_b & 0 \\ -V_2 & V_2 & R_2 I_b \end{bmatrix} \begin{bmatrix} D_1 \\ D_2 \\ D_4 \end{bmatrix} = \begin{bmatrix} V_1 + V_2 - V_{pv} \\ R_1 I_b \\ R_2 I_b \end{bmatrix}$$

$$(29)$$

The small signal converter model yields the following transfer function matrix for the converter:

$$G = C(SI - A)^{-1} B + D \quad (30)$$

where

$$y = Gu \quad (31)$$

The three transfer functions are represented as follows, where y and u are the respective output and input vectors of the system.

$$\frac{\hat{V}_1(s)}{d_4(s)} = g_{11}$$

$$\frac{\hat{V}_T(s)}{d_1(s)} = g_{22}$$

$$\frac{\hat{I}_b(s)}{d_2(s)} = g_{33} \quad (32)$$

It's also worth noting that in the charging of the battery, in the situation where the load power and battery current become low, the converter may switch to discontinuous conduction mode. The inductor current must be less than its current ripple for converters in DCM. The equations for the developed converter while charging the battery can be determined by making the voltage across the inductor and current through the capacitor at the switching period:

$$V_{bat}D_1 + (V_1 - V_{bat})D_2 + V_2D_4 = V_1 + V_2 - V_{pv}$$

$$-I_L D_2 + I_L = \frac{V_1}{R_1}$$

$$-I_L D_4 + I_L = \frac{V_2}{R_2} \quad (33)$$

In battery charging mode, the inductor current ripple can also be written as

$$\Delta I_L = \frac{V_{pv}D_1 T_s}{L} \quad (34)$$

As a result, if the following conditions are met, the converter will work in DCM from (28), (33), and (34).

$$I_L = \frac{V_2}{R_1(1-D_1)} < \frac{V_{pv}D_1T_s}{L}$$

$$I_L = \frac{V_2}{R_2(1-D_4)} < \frac{V_{pv}D_1T_s}{L}$$

$$I_L = \frac{I_b}{(D_2-D_1)} < \frac{V_{pv}D_1T_s}{L} \tag{35}$$

$$R_1 > \frac{V_1 L f_s}{D_1(1-D_2)V_{pv}}$$

$$R_2 > \frac{V_2 L f_s}{D_1(1-D_4)V_{pv}}$$

$$I_b > \frac{D_1(D_2-D_1)V_{pv}}{L f_s} \tag{36}$$

In reality, (36) verifies that when the battery charging current is low with light loading of output, the proposed converter will operate in DCM.

V. CONTROLLER DESIGN

The two operating modes and the respective transfer functions are initiated in the above sections. Because of the distinct transfer functions in both operating modes of the converter, a separate controller must be constructed for each model. Control block schematics of the converter in the two modes of operation are illustrated in FIGURE 10. $R_1 = R_2 = 35\Omega$ in battery discharging mode and $R_1 = R_2 = 70\Omega$ in the mode of charging the battery.

which (35) can be rewritten as in (37) and (38), shown at the bottom of the page.

A. CONTROLLER FOR BATTERY DISCHARGING MODE

There exist three transfer functions in this way as explained in Section IV. To construct the system compensators, computer software must obtain frequency-domain analysis for every transfer function. System compensators provide the appropriate steady-state error and the respective phase margin, as well as excellent stability and bandwidth. The transfer function of g_{11} is (37) given at the bottom of the page using the A, B, C, and D matrices shown in section IV and the transfer function of the respective matrix G.

The open-loop system of the bode diagram of g_{11} for the converter in its simulation parameters is represented in Table 2, designed using MATLAB software. FIGURE 11(a) and 11(b) depict bode diagrams. It can be

TABLE 2. Parameters of the converter.

Parameters	Ratings
Inductor, L	2.5mH
Capacitor, C_1	1000μF
Capacitor, C_2	1000μF
Solar PV voltage, V_{pv}	35V
Battery voltage, V_{bat}	48V
Switching frequency, F_s	10kHz
dSPACE controller	RTI1104

seen from the produced bode plots that the phase of the crossover frequency of g_{11} is $-179.99°$. As a result, the phase margin becomes insufficient, and the closed-loop system is inherently not stable. As a result, a lead compensator increases the phase margin and improves the stability of the system.

$$K(s) = K\frac{S+Z}{S+P} \tag{39}$$

K = 2.9, Z = 906.05 and P = 7641.6 in this equation. Bode graphs after adjustment are given in FIGURE 11(b). The system's stability has been improved by using a lead compensator. In addition, the transfer function of g_{22} is (34).

Bode graphs for g_{22} are shown in FIGURE 12(a) and 12(b). Bode diagrams reveal that the g_{22} phase margin is insufficient, necessitating the use of a lead compensator. As a result, a lead compensator is based on the utilization of the following transfer function.

$$K_{lead}(s) = 2.8960\frac{S+2098.9}{S+16982} \tag{40}$$

However, utilizing the lead compensator lowers the dc gain which increases the steady-state error. A lag compensator is to be incorporated into the given system to solve the problem. To avoid the lag compensator's effect on the lead compensator, the lag compensator zero is set ten times lower than the crossover frequency.

As a result, the lag transfer function is as follows:

$$K_{lag}(s) = K\frac{S+Z}{S+P} \tag{41}$$

where K = 1, P = 58.345, Z= 583.45. In FIGURE 12(b), bode plots after the application of compensation by using the lead-lag compensators are represented. Switch S_1 controls the current of source 2 (battery), as previously stated. In actuality, S_1 handles inductor current to set the battery current to the

$$g_{11} = \frac{\hat{V}_1(s)}{\hat{d}_4(s)} = \frac{\left(\frac{V_2(1-D_1)}{LC_1}\right)S + \left(\frac{V_2(1-D_1)}{LR_2C_1C_2} - \frac{I_L(1-D_1)(D_4-1)}{LC_1C_2}\right)}{S^3 + \left(\frac{R_1C_1+R_2C_2}{R_1R_2C_1C_2}\right)S^2 + \left(\frac{L+(1-D_1)^2R_1R_2C_2+(D_4-1)^2R_1R_2C_1}{LR_1R_2C_1C_2}\right)S + \left(\frac{R_1(1-D_1)^2+(D_4-1)^2R_2}{LR_1R_2C_1C_2}\right)} \tag{37}$$
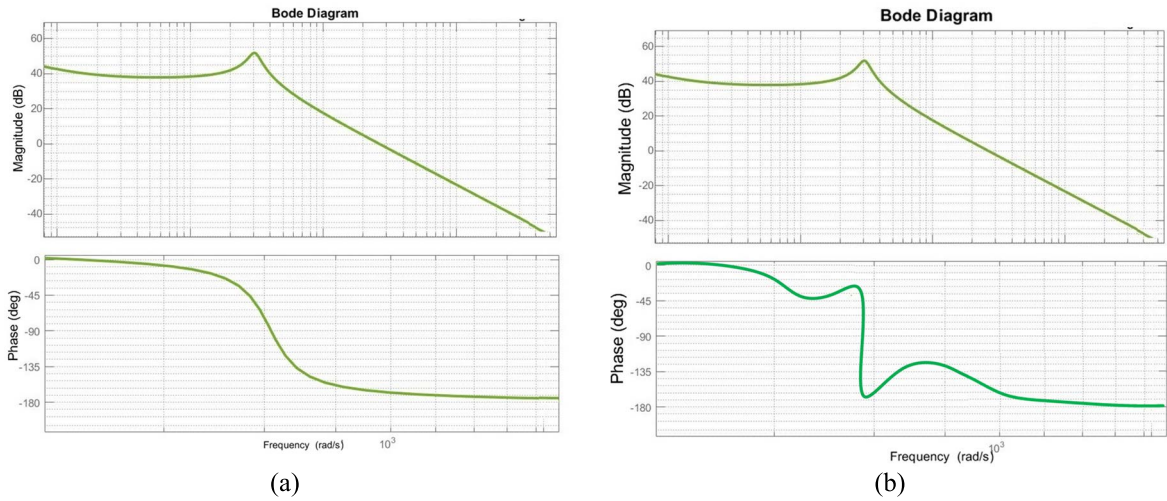
$$g_{22} = \frac{\hat{V}_T(s)}{\hat{d}_3(s)} = \frac{\left(\frac{V_{bat}-V_{pv}}{L}\right)\left(\frac{1-D_1}{C_1} - \frac{D_4-1}{C_2}\right)S + \left(\frac{1-D_1}{R_2C_1C_2} - \frac{D_4-1}{R_1C_1C_2}\right)\left(\frac{V_{bat}-V_{pv}}{L}\right)}{S^3 + \left(\frac{R_1C_1+R_2C_2}{R_1R_2C_1C_2}\right)S^2 + \left(\frac{L+(1-D_1)^2R_1R_2C_2+(D_4-1)^2R_1R_2C_1}{LR_1R_2C_1C_2}\right)S + \left(\frac{R_1(1-D_1)^2+(D_4-1)^2R_2}{LR_1R_2C_1C_2}\right)} \tag{38}$$

FIGURE 11. Simulations of the bode plots of g11 (s) (a) Before compensation (b) After applying the compensator.
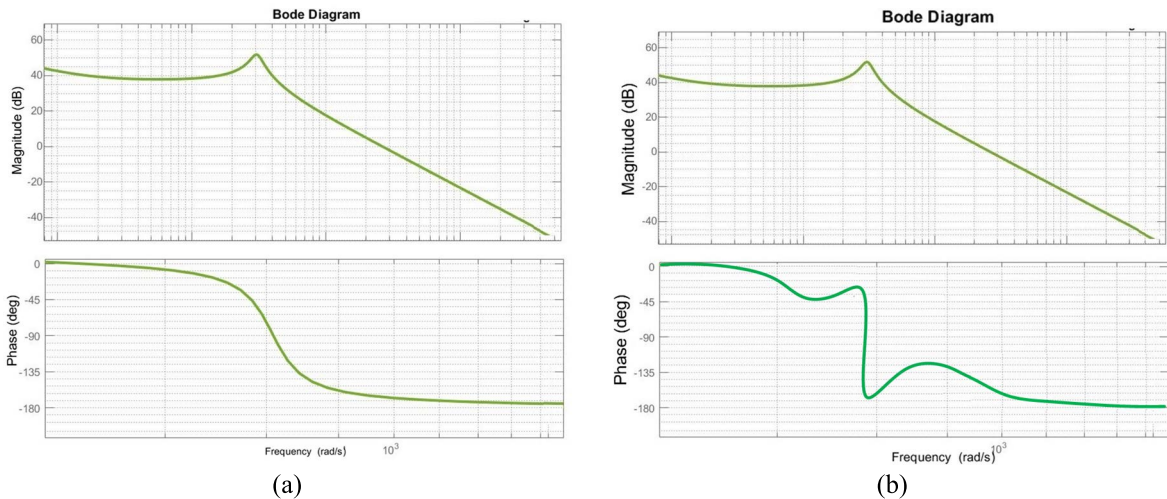

FIGURE 12. Simulations of the bode plots of g22 (s) (a) Before compensation (b) After applying the compensator.

required value, as illustrated in (42), as shown at the bottom of the page.

FIGURE 13(a) shows the g_{33} bode plot. As can be seen in the diagram, the phase margin is ample, resulting in a stable system with a low dc gain. As a result, the steady-state error is extremely valuable. A lag compensator is used to reduce steady-state inaccuracy.

$$K_{lag}(s) = \frac{S + 200}{S + 5} \tag{43}$$

Bode graphs after applying the lag compensator are presented in FIGURE 13(b).

B. CONTROLLER DESIGN FOR BATTERY CHARGING MODE

During this mode of operation, the switches S_1, S_2 and S_4 are turned on and S_3 is in an off state during this as described in the previous section. Switch S_4 is utilized to regulate the voltage output V_1. FIGURE 14 (a) shows the g_{11} bode diagram. A lead compensator is needed due to a lack of phase margin. As a result, the following transfer function is used to construct the lead compensator:

$$K_{lead}(s) = 2.9 \frac{S + 482.7}{S + 4065.8} \tag{44}$$

$$g_{33} = \frac{\hat{i}_b(s)}{\hat{d}_1(s)} = \frac{\left(\frac{V_1 D_3}{L}\right) S^2 + \left[\frac{D_3 V_1}{L}\left(\frac{1}{R_1 C_1} + \frac{1}{R_2 C_2}\right) + \frac{I_L(1-D_1)D_3}{LC_1}\right] S + \left(\frac{D_3 V_1}{LR_1 R_2 C_1 C_2} + \frac{I_L(1-D_1)D_3}{LR_2 C_1 C_2}\right)}{S^3 + \left(\frac{R_1 C_1 + R_2 C_2}{R_1 R_2 C_1 C_2}\right) S^2 + \left(\frac{L + (1-D_1)^2 R_1 R_2 C_2 + (D_4-1)^2 R_1 R_2 C_1}{LR_1 R_2 C_1 C_2}\right) S + \left(\frac{R_1(1-D_1)^2 + (D_4-1)^2 R_2}{LR_1 R_2 C_1 C_2}\right)} \tag{42}$$
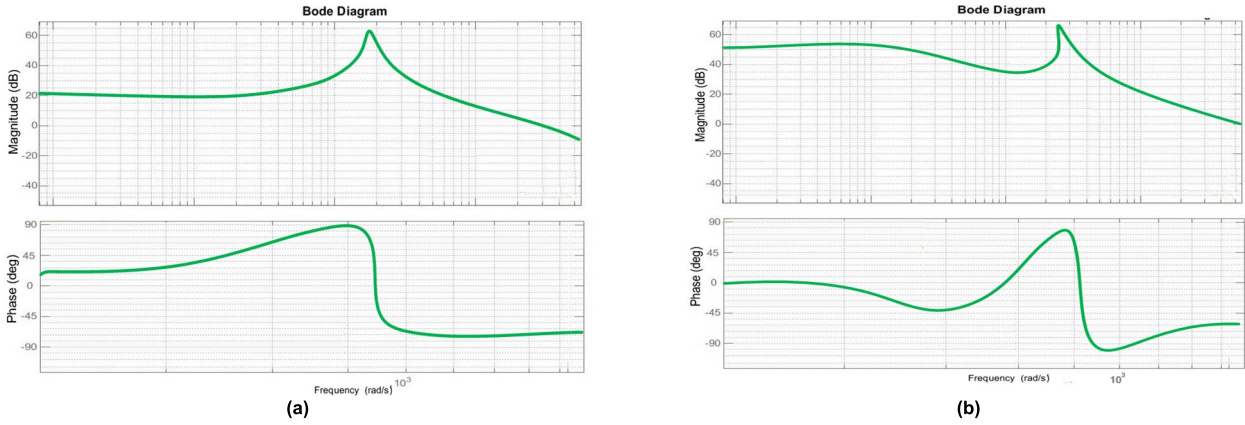
FIGURE 13. Simulations of the bode plots of g33 (s) (a) Before compensation (b) After applying the compensator.
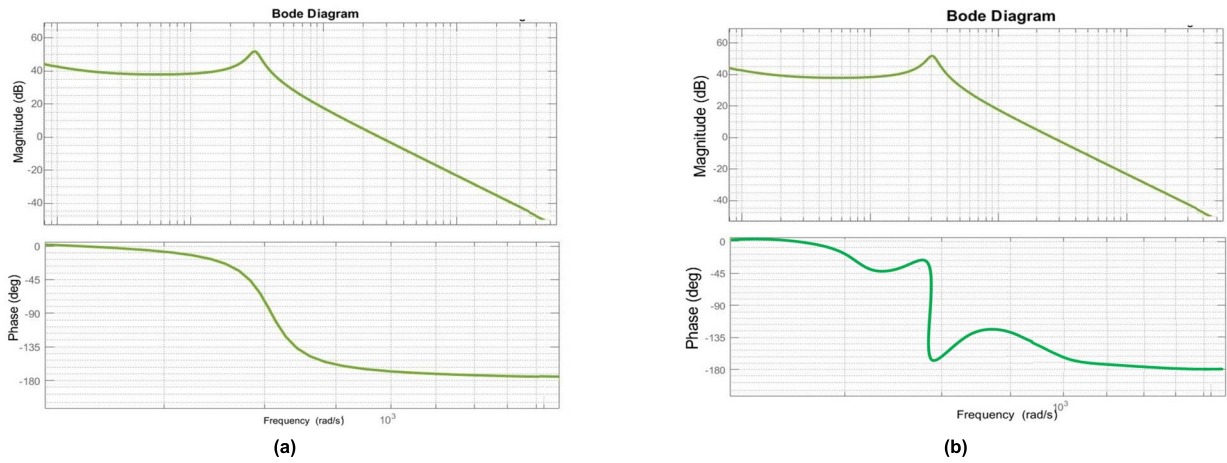

FIGURE 14. Simulations of the bode plot of g11 (s) (a) Before compensation (b) After applying the compensator.

A lag-type compensator is introduced to the proposed system to reduce steady-state error:

$$K_{lag}(s) = \frac{S + 140}{S + 14} \tag{45}$$

The bode plot after the application of the lead-lag compensator is illustrated in FIGURE 14(b). Switch S_1 is also utilized to regulate the total output voltage V_T in this operation mode. FIGURE 15(a) and 15(b) show the g_{22} bode diagram.

Because g_{22} phase margin is insufficient, the compensator utilized is represented below

$$K_{lead}(s) = 2.9\frac{S + 585.4}{S + 4937} \tag{46}$$

In addition, a lag compensator is used to reduce steady-state error:

$$K_{lag}(s) = \frac{S + 170}{S + 17} \tag{47}$$

The bode diagram after compensation is given in FIGURE 15(b). In addition, switch S_2 is utilized to regulate the battery charging current. FIGURE 16(a) and 16(b) show

the g_{33} bode diagram. The phase margin becomes sufficient and hence there will be no need for stabilizing the compensator, as shown in the diagram. Only a lag compensator is employed to reduce steady-state inaccuracy.

$$K_{lag}(s) = \frac{S + 267.4}{S + 2.67} \tag{48}$$

The bode diagram after compensation is given in FIGURE 16(b).

The inductor and capacitor values can be obtained using the following relations:

$$L = \frac{(V_{in} + V_b) \times d_2}{2 \times \Delta V_{01} \times f_s} \tag{49}$$

$$C_1 = C_2 = \frac{V_{01} \times d_1}{2 \times \Delta V_{01} \times f_s \times Z_{01}} \tag{50}$$

VI. RESULTS AND DISCUSSION
A. SIMULATION RESULTS
The performance of the developed converter is analyzed and designed using MATLAB software. The simulation parameters of the developed converter are shown in TABLE 2.
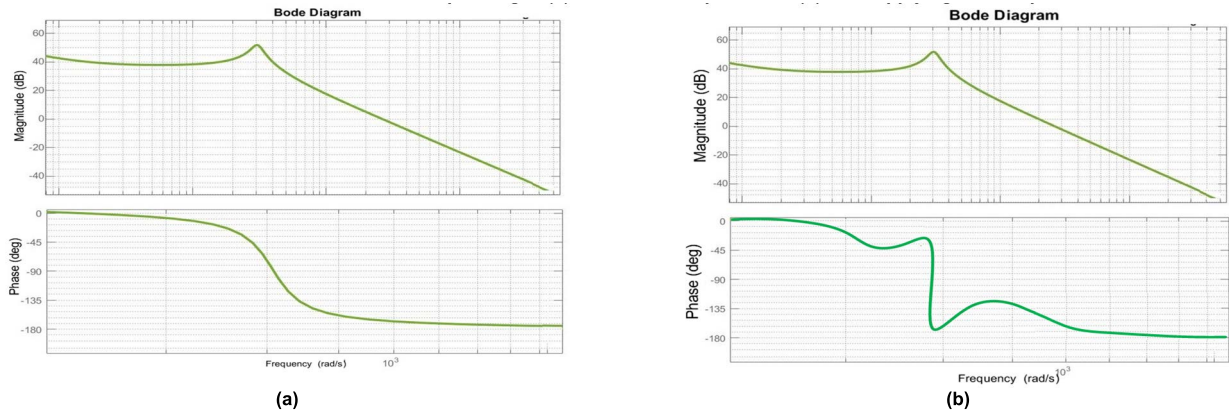
FIGURE 15. Simulations of the bode plot of g22 (s) (a) Before compensation (b) After applying the compensator.
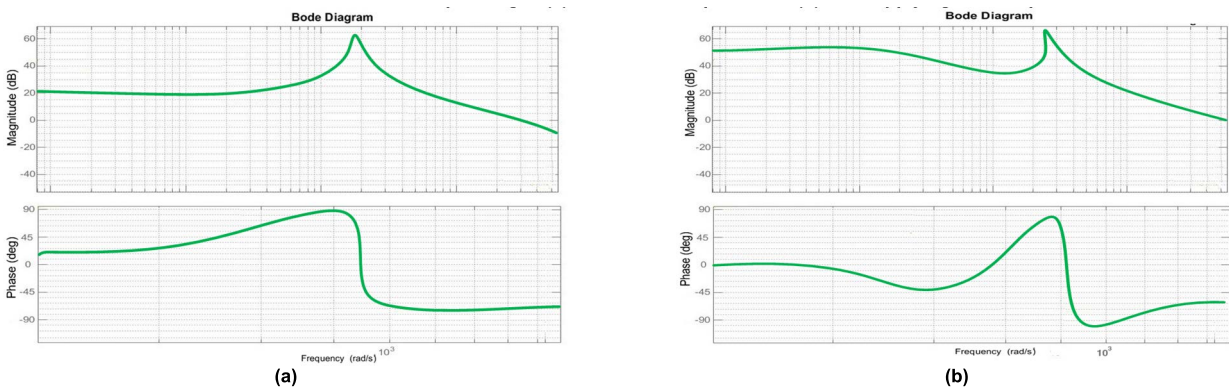

FIGURE 16. Simulations of the bode plot of g33 (s) (a) Before compensation (b) After applying the compensator.

$V_{pv} = 35V$, $V_{bat} = 48V$ are the input voltage sources. The battery model is utilized as an input source in simulation 2. The converter's output voltages should be regulated at $V_{1ref} = 80V$ and $V_{2ref} = 40V$. Hence, the total output voltage should be able to regulate at $V_{Tref} = 120V$. In addition, for battery discharge and charging modes, battery current should be regulated at $I_{bref} = 3A$ and $I_{bref} = 0.9A$, respectively. For the battery draining and charging modes $R_1 = R_2 = 35\Omega$ and $R_1 = R_2 = 70\Omega$ are the load resistances respectively.

Initially, the converter is in the discharging battery mode, with the switches S_1, S_3, and S_4 active, as shown in previous sections. Each switch is controlled by a compensator, which is built in Section V. FIGURE 17 depicts the output voltages V1 and VT. Regulating the output voltage represented yields the required values. FIGURE 18 depicts the battery current. The battery current is compared to the reference value. FIGURE 19 illustrates the inductor current. At a specific time ($t = 0.01s$), the battery source's reference current is abruptly increased from 3A to 4A. At a specific time ($t=0.07s$), the load power is abruptly increased.

Load resistances are modified to $R_1 = R_2 = 17.5\Omega$ at that moment. The respective change in the battery current is represented in FIGURE 20. As can be seen, controllers did an excellent job of regulating the battery current and the output
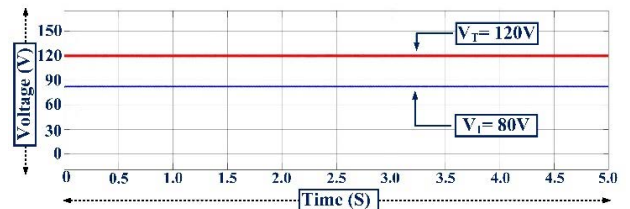

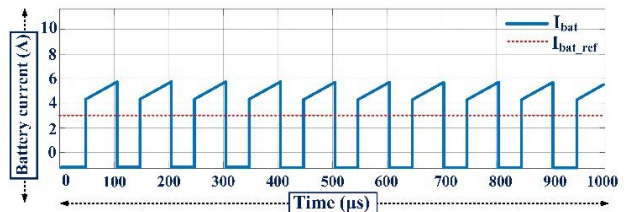**FIGURE 17.** Output voltages in battery discharging mode.

FIGURE 18. Output voltages in battery discharging mode.

voltages in response to load variations. In reality, the load power can be fed among the input sources by managing the battery current. In the charging mode of the battery, source 1
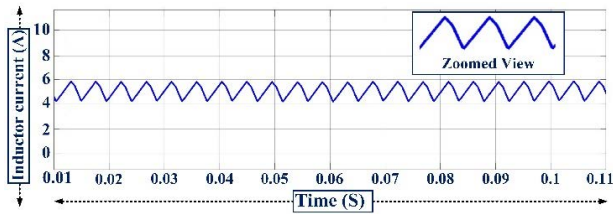
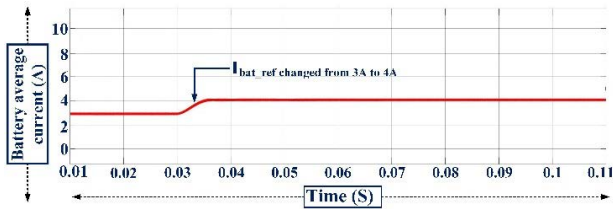**FIGURE 19.** Inductor current in discharging mode.
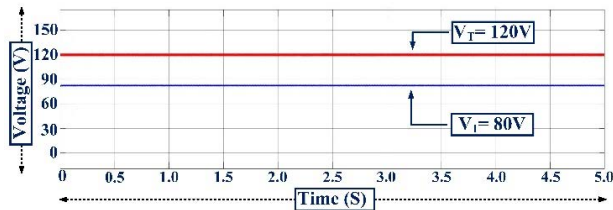

FIGURE 20. Change of battery reference current.

FIGURE 21. Output voltages in battery charging mode.
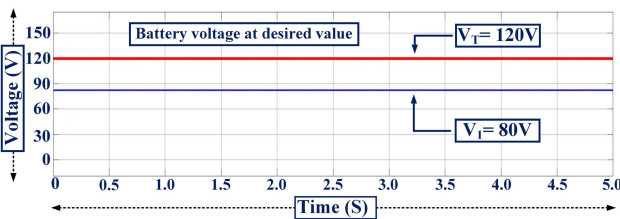

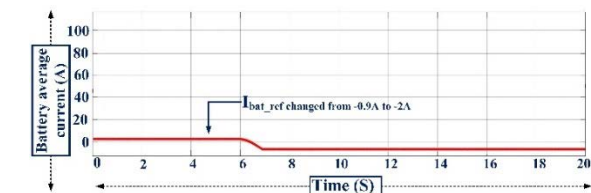**FIGURE 22.** Battery voltages at desired value.

FIGURE 23. Change of battery reference current.

supplies power to source 2 in addition to the loads (battery). Switches S_1, S_2 and S_4 are active in this mode. In this mode, the required output voltages are $V_{1ref} = 80V$, $V_{2ref} = 40V$ and the current reference of battery charging is $I_{bref} = 0.9A$, similar to the battery discharge mode.

In this case, the compensators created during the charging of the battery are used. FIGURE 21 depicts the respective

output port voltages V1 and VT. The reference values track the output voltages, as shown in this diagram. FIGURE 22 depicts the battery current after it has been adjusted to the desired value. The battery current is negative, indicating that the battery is being charged. The battery's reference current is rapidly reduced from −0.9 A to −2 A at a specific time (t = 6.5 s), as shown in FIGURE 23. Furthermore, at a predetermined time (t = 13s), the output load power is rapidly increased. In this case, the respective output voltages and battery current. The converter is well controlled by developed compensators, as can be seen in this diagram. It's important to note that every converter has a particular operating range.

B. EXPERIMENTAL RESULTS
The converter developed is designed in MATLAB/Simulink and tested in a laboratory environment with a hardware setup represented in FIGURE 31. Two separate power sources were used as inputs. In the setup, input sources are a dc power supply and a 48V battery consisting of four series 12V, 7.5Ah lead-acid batteries. The experimental specifications are shown in TABLE 2. The power supply is provided with a voltage of 35V the represents a solar PV voltage. The output voltages reference values are $V_{1ref} = 80V$ and $V_{2ref} = 40$ V respectively, and there use two resistive loads utilizing a dSPACE RTI1104 controller. The analysis is done in two separate converter operation modes. The following are detailed descriptions of the testing results for battery discharge as well as charging modes. At times before transition time, the converter is in battery discharging mode and after the transition time, the converter is in battery charging mode. It is obvious that against the operation mode changing and change of the loads the output voltages have been regulated to the desired values. The transition voltages from charging to discharging are represented in FIGURE 27.

1) BATTERY DISCHARGING MODE
The battery's reference current and output port voltages are defined in this mode as $I_{bref} = 3A$, $V_{1ref} = 80V$, and $V_{2ref} = 40V$, with $R_1 = R_2 = 35\Omega$ (less than 35). The output port voltages of the converter are displayed in FIGURE 24 under these conditions. The output port voltage V_1 and the total overall output port voltage $V_T = V_1 + V_2$ are displayed in this diagram. FIGURE 25 depicts the current fed from the battery and the inductor current. The current drawn by the battery is 3A. The correct distribution of power among the input energy sources can be achieved by managing the battery current. $P_{pv} = 150W$, $P_{bat} = 143W$, $P_1 = 189W$, and $P_2 = 47W$ in this mode.

2) BATTERY CHARGING MODE
The load power is modest in this mode. As a result, source 1 can both deliver loads by charging the battery. The output port voltages and the battery charging current is defined as $I_{bref} = 0.9A$, $V_{1ref} = 80V$, and $V_{2ref} = 40V$, respectively, as well as $R_1 = R_2 = 70\Omega$ (less than 70). The respective output port voltages of the developed converter are displayed
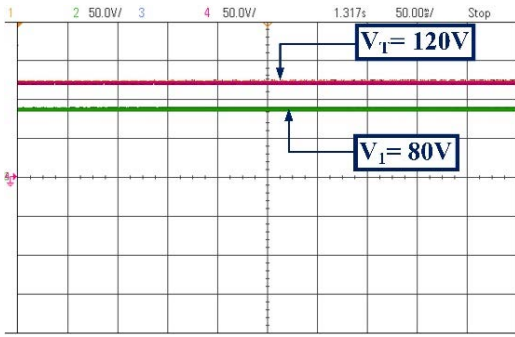
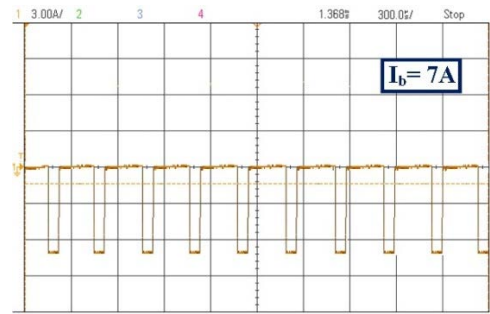**FIGURE 24.** Output voltages in battery discharging mode.

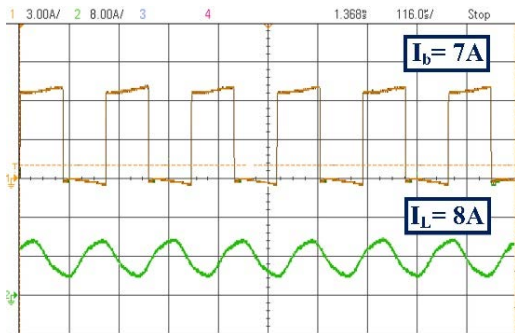**FIGURE 28.** Battery charging current.

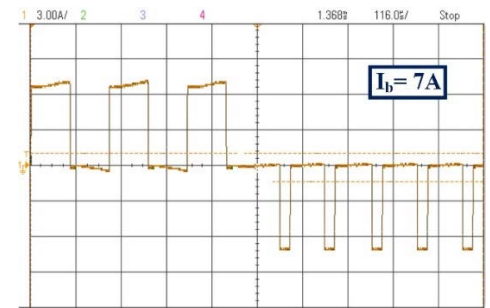**FIGURE 25.** Drawn current from battery and inductor current in discharging mode.

FIGURE 29. The battery current is discharging and the charging mode.
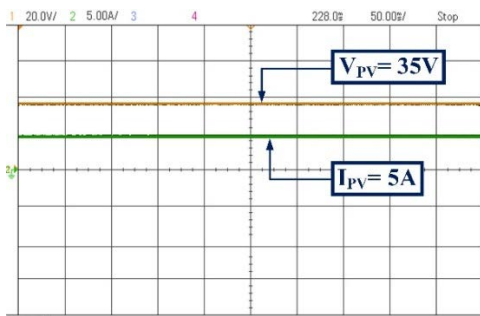
FIGURE 26. Solar PV voltage and current.
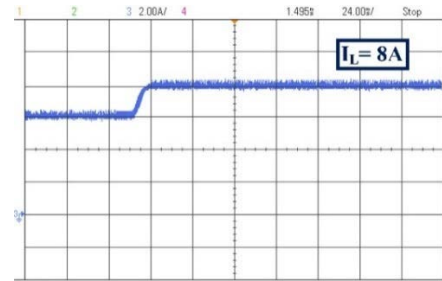
FIGURE 30. Variation of inductor current from battery discharging to charging.
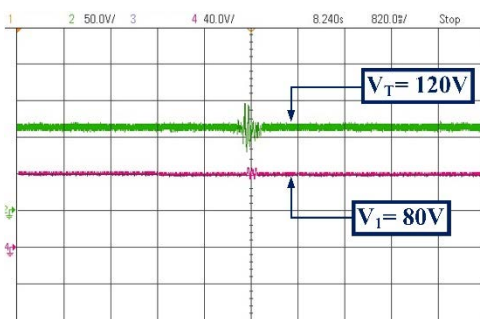
FIGURE 27. Output voltages of a converter.
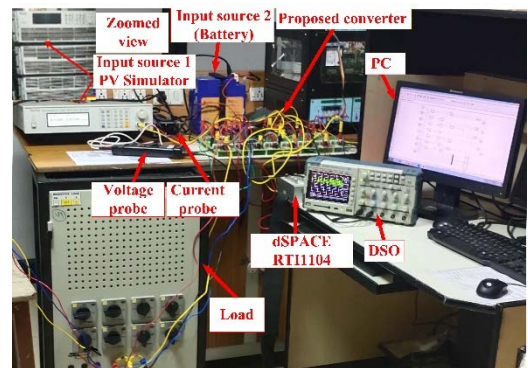
FIGURE 31. Experimental setup.

in FIGURE 27 under this circumstance. FIGURE 28 depicts the battery charging current. The current of source 1 equals the current of the inductor. $P_{pv} = 214W$, $P_{bat} = 51W$, $P_1 = 96W$, and $P_2 = 25W$ in this mode. The suggested converter's operation

from battery discharge to the battery charging mode is examined. The developed converter was initially made to run in battery discharge mode with the increase of load resistances

TABLE 3. Component comparison with existing topologies.

Topology	[4]	[7]	[8]	[13]	[14]	[18]	[20]	[25]	[26]	[28]	[29]	[31]	Proposed
Inputs	1	2	1	1	1	2	2	1	1	2	2	2	2
Outputs	1	2	1	1	1	1	1	1	2	2	2	2	2
Inductors	1	2	6	2	3	2	2	1	1	2	2	4	1
Switches	4	3	6	1	1	5	2	5	4	3	4	5	4
Diodes	-	2	-	2	2	2	3	5	-	5	4	5	4
Capacitors	3	3	4	3	4	1	2	2	2	1	2	5	2
Components count per ports	4	3.5	8	4	5	3.3	3	6.5	1.6	2.75	3	4.75	2.75
No. of operating modes	3	5	4	4	5	3	4	3	4	5	7	3	4
Circuit complexity	High	Low	High	Low	High	High	Low	High	Low	Low	High	High	Low
Devices conducted during operating modes	High	Low	Low	High	Low	High	Low	High	High	Low	High	High	Low
Power flow type from input to output	Shared	Shared	Shared	Shared	Separate	Separate	Shared	Separate	Shared	Shared	Shared	Shared	Shared
Extension of ports	Yes	Yes	Yes	Yes	Yes	Yes	Yes	Yes	Yes	Yes	Yes	Yes	Yes
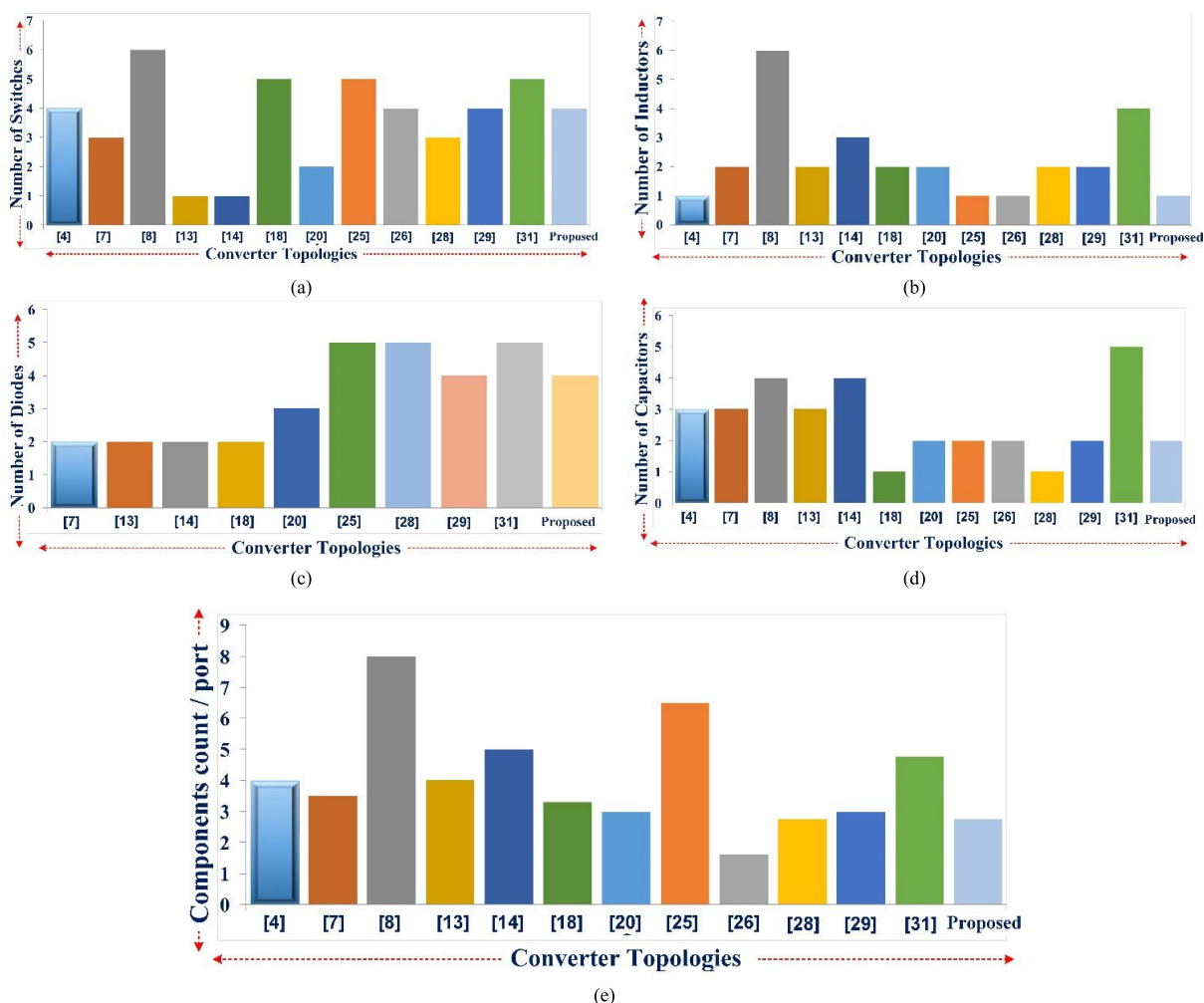
FIGURE 32. Comparison of various existing topologies with the proposed DIDO converter (a) NS, (b) ND, (c) NL (d) NC (e) CC/Port.

over time. Load resistances in discharge mode are $R_1 = R_2 = 35\Omega$, while load resistances in charging mode are $R_1 = R_2 = 70\Omega$. In addition, the reference current of the battery has been modified from 3A to -0.9A in battery discharging mode. Hence, the current through the battery during charging is displayed in FIGURE 28 under such conditions.

The converter is in battery draining mode before the transition time and battery charging mode after the transition time. The respective output port voltages have been controlled to the desired values in the face of shifting operation modes and changing loads. By shifting the mode of operation from charging to discharging, identical results can be produced. The battery current is displayed in FIGURE 29 as the mode changes from charging to discharging. The solar PV input voltage and respective current are represented in FIGURE 26. The variation of inductor current from battery discharging to charging is shown in FIGURE 30.

The proposed topology with passive elements and switches is compared to other similar converter topologies in Table 3. The results show that the suggested converters are comparable to that other converters. Furthermore, the suggested converter provides advantages such as a modular structure with fewer components and the integration of a variety of input sources with varying voltage-current characteristics. This converter can be used in electric vehicle power circuits. The proposed converter, in particular, can be used in a regenerative mode.

VII. CONCLUSION

This research proposes a multi-port converter with a combined structure for hybridizing power sources in the applications like electric vehicles. There is only one inductor in the proposed converter. The suggested converter can able to transfer energy among the various energies like solar PV and ESSs such as a battery. The power supply and ESS are referred to as solar PV source and battery respectively. The developed converter can also be used as a single-input, multi-output device. Multiple outputs with varying voltage levels are possible. In the battery discharge mode, input sources supply power to the output, whereas in the case of charging mode, out of the two inputs, one input source not only delivers power to loads but also provides to the battery. Transfer function matrices for each mode are computed individually, and the respective compensators utilized for closed-loop converter control are built. The battery current and the output voltages are regulated to desired values under various scenarios such as a quick rise in load power and a sudden shift in the battery reference current. Multilevel inverters can be connected to outputs with various voltage levels. Induction motor torque ripple is reduced when multilayer inverters are used in electric automobiles. However, electric vehicles have at least two separate dc voltages, one for cabin lighting and the other for the motor. Multilevel inverters are also beneficial in grid connectivity of renewable energy resources like solar PV. Finally, the operation of this converter is tested in the laboratory using a hardware setup.

REFERENCES

[1] S. R. Khasim and C. Dhanamjayulu, "Selection parameters and synthesis of multi-input converters for electric vehicles: An overview," *Renew. Sustain. Energy Rev.*, vol. 141, May 2021, Art. no. 110804, doi: 10.1016/j.rser.2021.110804.

[2] P.-J. Liu, Y.-K. Lo, H.-J. Chiu, and Y.-J. Emery Chen, "Dual-current pump module for transient improvement of step-down DC–DC converters," *IEEE Trans. Power Electron.*, vol. 24, no. 4, pp. 985–990, Apr. 2009, doi: 10.1109/TPEL.2008.2010322.

[3] J. Macaulay and Z. Zhou, "A fuzzy logical-based variable step size P&O MPPT algorithm for photovoltaic system," *Energies*, vol. 11, no. 6, p. 1340, May 2018, doi: 10.3390/en11061340.

[4] M. Dhananjaya, D. Ponuru, T. S. Babu, B. Aljafari, and H. H. Alhelou, "A new multi-output DC-DC converter for electric vehicle application," *IEEE Access*, vol. 10, pp. 19072–19082, 2022.

[5] L. Wang, E. G. Collins, and H. Li, "Optimal design and real-time control for energy management in electric vehicles," *IEEE Trans. Veh. Technol.*, vol. 60, no. 4, pp. 1419–1429, May 2011, doi: 10.1109/TVT.2011.2122272.

[6] M. Zandi, A. Payman, J. P. Martin, S. Pierfederici, B. Davat, and F. Meibody-Tabar, "Energy management of a fuel cell/supercapacitor/battery power source for electric vehicular applications," *IEEE Trans. Veh. Technol.*, vol. 60, no. 2, pp. 433–443, Nov. 2011, doi: 10.1109/TVT.2010.2091433.

[7] K. Suresh, C. Bharatiraja, N. Chellammal, M. Tariq, R. K. Chakrabortty, M. J. Ryan, and B. Alamri, "A multifunctional non-isolated dual input-dual output converter for electric vehicle applications," *IEEE Access*, vol. 9, pp. 64445–64460, 2021.

[8] S. R. Khasim and C. Dhanamjayulu, "Design and implementation of asymmetrical multilevel inverter with reduced components and low voltage stress," *IEEE Access*, vol. 10, pp. 3495–3511, 2022, doi: 10.1109/ACCESS.2022.3140354.

[9] A. Ajami, H. Ardi, and A. Farakhor, "A novel high step-up DC/DC converter based on integrating coupled inductor and switched-capacitor techniques for renewable energy applications," *IEEE Trans. Power Electron.*, vol. 30, no. 8, pp. 4255–4263, Aug. 2015, doi: 10.1109/TPEL.2014.2360495.

[10] M. R. Banaei, H. Ardi, R. Alizadeh, and A. Farakhor, "Non-isolated multi-input-single-output DC/DC converter for photovoltaic power generation systems," *IET Power Electron.*, vol. 7, no. 11, pp. 2806–2816, Nov. 2014, doi: 10.1049/iet-pel.2013.0977.

[11] O. Hegazy, R. Barrero, J. Van Mierlo, P. Lataire, N. Omar, and T. Coosemans, "An advanced power electronics interface for electric vehicles applications," *IEEE Trans. Power Electron.*, vol. 28, no. 12, pp. 5508–5521, Dec. 2013, doi: 10.1109/TPEL.2013.2256469.

[12] C. Dhanamjayulu, S. Padmanaban, V. K. Ramachandaramurthy, J. B. Holm-Nielsen, and F. Blaabjerg, "Design and implementation of multilevel inverters for electric vehicles," *IEEE Access*, vol. 9, pp. 317–338, 2021.

[13] Y. Cao and J. A. Abu Qahouq, "Evaluation of bi-directional single-inductor multi-input battery system with state-of-charge balancing control," *IET Power Electron.*, vol. 11, no. 13, pp. 2140–2150, Nov. 2018.

[14] S. R. Khasim, D. C, S. Padmanaban, J. B. Holm-Nielsen, and M. Mitolo, "A novel asymmetrical 21-level inverter for solar PV energy system with reduced switch count," *IEEE Access*, vol. 9, pp. 11761–11775, 2021, doi: 10.1109/ACCESS.2021.3051039.

[15] R. Ahmadi and M. Ferdowsi, "Double-input converters based on H-bridge cells: Derivation, small-signal modeling, and power sharing analysis," *IEEE Trans. Circuits Syst. I, Reg. Papers*, vol. 59, no. 4, pp. 875–888, Apr. 2012, doi: 10.1109/TCSI.2011.2169910.

[16] L. Solero, A. Lidozzi, and J. A. Pomilio, "Design of multiple-input power converter for hybrid vehicles," *IEEE Trans. Power Electron.*, vol. 20, no. 5, pp. 1007–1016, Sep. 2005, doi: 10.1109/TPEL.2005.854020.

[17] B. Faridpak, M. Farrokhifar, M. Nasiri, A. Alahyari, and N. Sadoogi, "Developing a super-lift luo-converter with integration of buck converters for electric vehicle applications," *CSEE J. Power Energy Syst.*, vol. 7, no. 4, pp. 811–820, 2020.

[18] S. R. Khasim and D. C, "Design of multiple input DC–DC converters for interfacing solar/fuel cell/battery electric vehicles," in *Proc. Innov. Power Adv. Comput. Technol. (i-PACT)*, Nov. 2021, pp. 1–7.

[19] C. Dhanamjayulu, S. R. Khasim, S. Padmanaban, G. Arunkumar, J. B. Holm-Nielsen, and F. Blaabjerg, "Design and implementation of multilevel inverters for fuel cell energy conversion system," *IEEE Access*, vol. 8, pp. 183690–183707, 2020, doi: 10.1109/access.2020.3029153.

[20] K. Suresh, N. Chellammal, C. Bharatiraja, P. Sanjeevikumar, F. Blaabjerg, and J. B. H. Nielsen, "Cost-efficient nonisolated three-port DC–DC converter for EV/HEV applications with energy storage," *Int. Trans. Electr. Energy Syst.*, vol. 29, no. 10, p. e12088, Oct. 2019.

[21] C. Dhanamjayulu, D. Prasad, S. Padmanaban, P. K. Maroti, J. B. Holm-Nielsen, and F. Blaabjerg, "Design and implementation of seventeen level inverter with reduced components," *IEEE Access*, vol. 9, pp. 16746–16760, 2021, doi: 10.1109/ACCESS.2021.3054001.

[22] Y.-C. Liu and Y.-M. Chen, "A systematic approach to synthesizing multi-input DC–DC converters," *IEEE Trans. Power Electron.*, vol. 24, no. 1, pp. 116–127, Jan. 2009, doi: 10.1109/TPEL.2008.2009170.

[23] H. Wu, K. Sun, S. Ding, and Y. Xing, "Topology derivation of non-isolated three-port DC–DC converters from DIC and DOC," *IEEE Trans. Power Electron.*, vol. 28, no. 7, pp. 3297–3307, Jul. 2013, doi: 10.1109/TPEL.2012.2221746.

[24] B. N. Alajmi, M. I. Marei, I. Abdelsalam, and N. A. Ahmed, "Multi-phase interleaved converter based on cascaded non-inverting buck-boost converter," *IEEE Access*, vol. 10, pp. 42497–42506, 2022.

[25] B. N. Alajmi, M. I. Marei, I. Abdelsalam, and M. F. AlHajri, "Analysis and design of a multi-port DC–DC converter for interfacing PV systems," *Energies*, vol. 14, no. 7, p. 1943, Apr. 2021.

[26] K. Shreya, H. Srivastava, P. Kumar, G. Ramanathan, P. Madhavan, and C. Bharatiraja, "CUK converter fed resonant LLC converter based electric bike fast charger for efficient CC/CV charging solution," *J. Appl. Sci. Eng.*, vol. 24, no. 3, pp. 331–338, 2021.

[27] B. Axelrod, Y. Berkovich, and A. Ioinovici, "Continuous-time digital controller," in *Proc. Int. Symp. Circuits Syst. (ISCAS)*, vol. 3, no. 2, Jun. 2003, pp. 564–573.

[28] S. Athikkal, B. Chokkalingam, S. I. Ganesan, B. Lehman, and T. B. Lazzarin, "Performance evaluation of a dual-input hybrid step-up DC–DC converter," *IEEE Trans. Ind. Appl.*, vol. 58, no. 3, pp. 3769–3782, Jun. 2022.

[29] F. Kardan, R. Alizadeh, and M. R. Banaei, "A new three input DC/DC converter for hybrid PV/FC/Battery applications," *IEEE J. Emerg. Sel. Topics Power Electron.*, vol. 5, no. 4, pp. 1771–1778, Dec. 2017.

[30] M. AL-Emam, M. I. Marei, and W. El-khattam, "A maximum power point tracking technique for PV under partial shading condition," in *Proc. 8th IEEE India Int. Conf. Power Electron. (IICPE)*, Dec. 2018, pp. 1–6.

[31] P. Mohseni, S. H. Hosseini, M. Sabahi, T. Jalilzadeh, and M. Maalandish, "A new high step-up multi-input multi-output DC–DC converter," *IEEE Trans. Ind. Electron.*, vol. 66, no. 7, pp. 5197–5208, Sep. 2018.

[32] N. Asim, K. Sopian, S. Ahmadi, K. Saeedfar, M. A. Alghoul, O. Saadatian, and S. H. Zaidi, "A review on the role of materials science in solar cells," *Renew. Sustain. Energy Rev.*, vol. 16, no. 8, pp. 5834–5847, 2012, doi: 10.1016/j.rser.2012.06.004.

[33] A. Amir, A. Amir, J. Selvaraj, and N. A. Rahim, "Study of the MPP tracking algorithms: Focusing the numerical method techniques," *Renew. Sustain. Energy Rev.*, vol. 62, pp. 350–371, Sep. 2016, doi: 10.1016/j.rser.2016.04.039.

C. DHANAMJAYULU (Senior Member, IEEE) received the B.Tech. degree in electronics and communication engineering from JNTU University, Hyderabad, India, the M.Tech. degree in control and instrumentation systems from the IIT Madras, Chennai, India, and the Ph.D. degree in power electronics from the Vellore Institute of Technology, Vellore, India. He was invited as a Visiting Researcher with the Department of Energy Technology, Aalborg University, Esbjerg, Denmark, funded by the Danida Mobility Grant, Ministry of Foreign Affairs of Denmark on Denmark's International Development Cooperation. He was a Postdoctoral Fellow at the Department of Energy Technology, Aalborg University, from October 2019 to January 2021. Since 2010, he has been a Senior Assistant Professor with the Vellore Institute of Technology. His research interests include multilevel inverters, power converters, active power filters, power quality, grid-connected systems, smart grids, electric vehicle, electric spring, and tuning of memory elements and controller parameters using softswitching techniques for power converters, average modeling, steady-state modeling, and small-signal modeling stability analysis of the converters and inverters. He is an Academic Editor of the *Journal International Transactions on Electrical Energy Systems* (Wiley-Hindawi). He is also an Academic Editor of the *Journal Mathematical Problems in Engineering* (Hindawi).

SHAIK REDDI KHASIM (Member, IEEE) received the B.Tech. degree (Hons.) in electrical engineering and the M.Tech. degree (Hons.) from JNTUA, Andhra Pradesh, India, in 2012 and 2015, respectively. He is currently pursuing the Ph.D. degree in power electronics with the Vellore Institute of Technology, Vellore, India. His research interests include multilevel inverters, power converters, and electric vehicles.

S. M. MUYEEN (Senior Member, IEEE) received the B.Sc.Eng. degree from the Rajshahi University of Engineering and Technology (RUET), Bangladesh, formerly known as the Rajshahi Institute of Technology, in 2000, and the M.Eng. and Ph.D. degrees from the Kitami Institute of Technology, Japan, in 2005 and 2008, respectively, all in electrical and electronic engineering. He is a Full Professor with the Electrical Engineering Department, Qatar University. He is a keynote speaker and an invited speaker at many international conferences, workshops, and universities. He has published more than 350 articles in different journals and international conferences. He has published seven books as an author or editor. His research interests include power system stability and control, electrical machine, FACTS, energy storage systems (ESS), renewable energy, and HVDC systems. He is a Senior Member of Chartered Professional Engineers, Australia, and a fellow of Engineers Australia. He is serving as the Editor/an Associate Editor for many prestigious journals from IEEE, IET, and other publishers, including IEEE Transactions on Energy Conversion, IEEE Power Engineering Letters, *IET Renewable Power Generation*, and *IET Generation, Transmission and Distribution*.

• • •